ARTICLE

Ligand-engineered ZnS quantum dots synthesized from substituted thioureas: scalable production, polymer grafting, and emissive film fabrication

Received 00th January 20xx,
Accepted 00th January 20xx

DOI: 10.1039/x0xx00000x

Jiri Jemelka[a,b], Liudmila Loghina[b]*, Bozena Frumarova[b], Jhonatan Rodriguez-Pereira[b], Stanislav Slang[b], Jakub Houdek[b], Michal Kurka[b], Roman Jambor[c], and Miroslav Vlcek[b,c]

Zinc sulfide (ZnS) quantum dots (QDs) were synthesized using a series of substituted thioureas as single-source sulfur precursors in a high-temperature 1-octadecene medium. The hot-injection method offered excellent reproducibility and enabled straightforward scale-up to multigram quantities without compromising particle size or optical characteristics. The as-prepared ZnS QDs exhibited a high organic content (~46 wt.%), originating from in situ-generated surface ligands, which was quantitatively determined through acid digestion. This surface composition provided a versatile platform for subsequent ligand exchange. Functional ligands, including 2-mercaptopropionic acid (2-MPA), bis[2-(methacryloyloxy)ethyl] phosphate (BMEP), and 10-(phosphonooxy)decyl methacrylate (PODM), were successfully introduced, yielding hydrophilic, hydrophobic, and polymer-reactive ZnS QDs. Structural analysis (XRD, STEM, EDS, FTIR, XPS) confirmed the formation of cubic ZnS QDs with uniform particle sizes (6-8 nm) and verified the incorporation of the new ligands without altering the ZnS core. Optical measurements revealed size-dependent absorption and emission properties across the thiourea series, as well as pronounced ligand-dependent modulation of photoluminescence intensity and decay kinetics. Finally, pristine and functionalized QDs were incorporated into PMMA, PVK, PEG, and methacrylate-based copolymers to form uniform emissive thin films, with AFM demonstrating smooth surface morphology for most systems. These results establish substituted thioureas as effective precursors for scalable ZnS QD synthesis and highlight ligand engineering as a powerful tool for tuning surface chemistry and enabling direct polymer integration.

Introduction

Zinc sulfide (ZnS) quantum dots (QDs) are among the most attractive metal chalcogenide nanomaterials owing to their wide bandgap, low toxicity, and high chemical stability. Their potential for optoelectronic applications, including light-emitting devices, sensors, and bioimaging agents, is significantly determined by surface chemistry and the choice of synthetic routes.[1-5] ZnS QDs have been investigated as environmentally benign alternatives to cadmium-based materials, offering good photoluminescence and stability under appropriate surface passivation. Despite these advantages, significant synthetic challenges persist in achieving precise control over size, dispersity, and surface properties, particularly for large-scale and functional applications.[6-8]

Traditionally, ZnS QDs are synthesized using a variety of sulfur sources, including alkyl thiols, thioacetamide (TAA), elemental sulfur, and H_2S gas. Among these, thioacetamide and elemental sulfur are the most commonly employed due to their ready availability and straightforward thermal decomposition. TAA, for example, is widely used in aqueous-phase syntheses of ZnS and ZnS-based core/shell QDs, often in combination with zinc acetate or zinc nitrate, under reflux or hydrothermal conditions.[9] However, the decomposition of TAA typically proceeds via a multi-step mechanism, releasing sulphide ions slowly and resulting in broader size distributions and less crystalline particles.

Elemental sulfur has also been employed as a sulfur precursor for ZnS QDs, particularly in hot-injection methods. In such protocols, sulphur is typically dissolved in coordinating solvents such as oleylamine or trioctylphosphine (TOP), which facilitate its gradual reduction and integration into growing nanocrystals.[10,11] While this method can yield monodisperse particles, it often requires long reaction times and elevated temperatures. For example, several studies have demonstrated the formation of ZnS and ZnS-based alloy nanocrystals through thermal decomposition of sulfur dissolved in oleylamine or by stepwise injection of sulfur precursors under an inert atmosphere. These approaches provide size control and good crystallinity but may involve complex precursor handling and limited functional group compatibility.[12] Dodecanethiol (DDT) is

[a] Institute of Applied Physics and Mathematics, Faculty of Chemical Technology, University of Pardubice, Studentska 95, Pardubice 53210, Czech Republic.
[b] Center of Materials and Nanotechnologies, Faculty of Chemical Technology, University of Pardubice, nam. Cs. legii 565, Pardubice 53002, Czech Republic.
[c] Department of General and Inorganic Chemistry, Faculty of Chemical Technology, University of Pardubice, Studentska 95, Pardubice 53210, Czech Republic.
* Corresponding author, email: liudmila.loghina@upce.cz.
Supplementary Information available: [synthesis details, EDS spectra, size distribution histograms, and additional optical and AFM data]. See DOI: 10.1039/x0xx00000x

another frequently used sulfur source that also acts as a surface ligand, particularly in nonpolar solvents such as octadecene. While DDT facilitates the formation of well-passivated nanocrystals, its strong surface binding can impede further ligand exchange and post-synthetic surface engineering.[13]

Recent reports have also explored the use of alternative sulfur precursors such as sodium sulphide, thiourea, and organic dithiocarbamates, which offer improved control over reactivity and compatibility with low-temperature aqueous synthesis routes.[14,15] These advances underscore the growing interest in tunable, low-toxic sulfur sources for more reproducible and scalable synthesis of ZnS QDs with controlled surface chemistry and narrow size distributions. Nevertheless, many of these approaches remain limited to binary sulfur sources and lack versatility for post-functionalization, motivating further exploration of ligand-bearing or multifunctional precursors. In recent years, substituted thioureas have emerged as efficient and tunable sulfur precursors for the synthesis of ternary I-III-VI nanocrystals, such as $AgInS_2$.[16] However, to our knowledge, no studies have applied this strategy to the synthesis of binary ZnS QDs, despite its potential to introduce unique ligand-surface interactions and enhance functionalization versatility.

Here, we investigate this relationship by synthesizing ZnS QDs from a diverse set of substituted thioureas under high-temperature hot-injection conditions. This approach enables rapid and homogeneous nucleation, yielding nearly monodisperse ZnS nanocrystals with particle sizes of 6-8 nm. The method is robust and reproducible, and importantly, it can be scaled up to multigram batches without changes in morphology or optical properties. The as-prepared QDs contain a high fraction of surface-bound organic material, originating exclusively from zinc linoleate species formed during precursor conversion. Quantification of this organic shell provides a direct basis for controlled surface engineering. Using this platform, we introduce three functional capping ligands: 2-mercaptopropionic acid (2-MPA), bis[2-(methacryloyloxy)ethyl] phosphate (BMEP), and 10-(phosphonooxy)decyl methacrylate (PODM), and examine how each ligand influences the structure, composition, and photophysical behaviour of ZnS QDs. The extensive analysis using XRD, STEM, EDS, FTIR, and XPS techniques demonstrates that the ZnS core remains intact, while the surface chemistry can be selectively tuned without inducing degradation or oxidation. Optical measurements reveal clear correlations between ligand identity and photoluminescence efficiency, exciton relaxation pathways, and Stokes shifts.

Finally, by exploiting ligand polarity and polymer-reactive functional groups, we incorporated the ZnS QDs into multiple polymer matrices (PMMA, PVK, PEG, and latex) and also performed radical copolymerization with vinyl monomers. These stable hybrid materials were deposited onto a glass surface, and their optical properties, together with surface morphology, were evaluated, demonstrating successful integration of the nanocrystals into functional polymer systems. Together, these results establish substituted thioureas as versatile precursors for ZnS nanocrystals and highlight ligand engineering as a powerful tool for tailoring surface chemistry and enabling polymer-compatible optical materials.

Experimental

Materials and reagents

Zinc oxide (ZnO, 99%), linoleic acid (LA, technical grade, 60-74%), 1-octadecene (ODE, technical grade, 90%), phenyl isothiocyanate (98%), allyl isothiocyanate (95%), octylamine (99%), benzylamine (99%), allylamine (99%), piperidine (99%), morpholine (99%), diethylamine (99%) oleylamine (OAm, technical grade, 70%), 2,4,6-trichloro-1,3,5-triazine (TCT, 99%), chloroform-d ($CDCl_3$, 99.8 atom% D), polyethylene glycol (PEG, Mn 6,000), polymethyl methacrylate (PMMA), polyvinyl carbazole (PVK), methacrylate, vinyl carbazole, 2,2'-azobis(2-methylpropionitrile) (AIBN) and silica gel (high-purity grade, pore size: 60 Å; particle size: 230-400 mesh) were purchased from Sigma-Aldrich and used without further purification. Sodium hydroxide (NaOH, p.a.), hydrochloric acid (HCl, 35%), and solvents were purchased from Penta (Czech Republic) and used for the purification of organic precursors and nanocrystals. Tetramethylammonium hydroxide (TMAH, 25% in methanol), 2-mercaptopropionic acid (2-MPA, 99%), bis[2-(methacryloyloxy)ethyl] phosphate (BMEP), and 10-(phosphonooxy)decyl methacrylate (PODM) were used as received. All reactions involving moisture- or air-sensitive materials were performed under a dry argon atmosphere using standard Schlenk techniques.

Synthesis of ZnS quantum dots using substituted thioureas

Typical procedure for the preparation of di- and trisubstituted thioureas. Substituted di- and trisubstituted thioureas were synthesized by reacting the appropriate isothiocyanate (0.05 mol) with the corresponding amine (0.055 mol) in dry benzene (75 ml) at ambient temperature under continuous stirring. The amine was added in three portions over the first 30 minutes. The reaction mixture was stirred for 1-3 h, and the reaction progress was monitored by thin-layer chromatography (TLC). Upon completion, the solvent was removed under reduced pressure using a rotary evaporator. The crude products were used in subsequent steps without additional purification. The prepared substituted thioureas and synthesized isothiocyanate precursors were characterized by NMR spectroscopy, and the gathered spectra are provided in the *Supplementary Materials*.

Structures and analytical data for the synthesized thioureas are provided in the *Supplementary Materials*. The set includes: 1-allyl-3-octylthiourea (**TU1**), 1-octyl-3-piperidinethiourea (**TU2**), 1-phenyl-3-octylthiourea (**TU3**), 1-phenyl-3-morpholinethiourea (**TU4**), 1-phenyl-3-oleylthiourea (**TU5**), 1-dodecyl-3-octylthiourea (**TU6**), 1-dodecyl-3-piperidinethiourea (**TU7**), 1-benzyl-3-allylthiourea (**TU8**), 1-benzyl-3-morpholinethiourea (**TU9**), 1,3-dioctylthiourea (**TU10**) and 3-allyl-1,1-diethylthiourea (**TU11**).

Hot-injection synthesis of ZnS QDs using substituted thioureas. ZnO (0.814 g, 0.01 mol), linoleic acid (9.33 ml, 0.03 mol), and ODE (15 ml) were added to a Schlenk flask and degassed under vacuum with argon backfilling at 100 °C for 1-

1.5 h. During this time, the mixture was stirred vigorously to ensure homogenization and complete conversion of ZnO into zinc linoleate. After removal of water and residual gases, the reaction temperature was raised to 240 °C and stabilized. A freshly prepared solution of substituted thiourea (0.025 mol) in 2 ml ODE and 1 ml oleylamine was rapidly injected into the hot reaction mixture. The reaction was maintained at 240 °C for 25 min to allow stable nanocrystal growth. After that, heating was discontinued, and the mixture was allowed to cool spontaneously to room temperature. To isolate the nanocrystals, the cooled colloidal solution was transferred into an equal volume of chloroform. ZnS QDs were then precipitated by the gradual addition of acetone (approx. 50 ml), followed by centrifugation at 6000 rpm for 5 min. The supernatant was decanted, and the precipitate was redispersed in a minimal amount of chloroform and reprecipitated with acetone. The cleaning cycle was repeated to ensure the removal of unreacted precursors and residual solvents. The final product was dried under vacuum at 50 °C for 3 h. Typical yield was 0.6-0.8 g per batch.

*Large-scale synthesis of ZnS QDs using **TU5***. A scale-up of the reaction was performed using **TU5** as the sulfur precursor. The synthesis was carried out in a three-neck round-bottom flask connected to an argon line, equipped with an air condenser and a thermometer. All reagent quantities were increased fivefold, and the procedure for QDs formation, isolation, and purification was identical to the standard-scale synthesis. The resulting batch yielded 4.6 g of ZnS QDs as a dry powder.

Determination of ligand content via acid digestion. To estimate the organic ligand content, ZnS QDs (0.20 g) were treated with 10% aqueous HCl (15 ml) under magnetic stirring at room temperature until complete dissolution of the solid phase (approximately 2 h). The resulting aqueous mixture was extracted with diethyl ether (3 × 20 ml), and the combined organic layers were washed with brine and dried over anhydrous Na_2SO_4. The ether solution was filtered into a pre-weighed round-bottom flask and evaporated using a rotary evaporator. The remaining residue was dried under vacuum for 1 h and weighed. The final mass of the organic fraction was attributed to surface-bound ligands removed from the nanocrystal surface. For ZnS QDs obtained via the large-scale synthesis (**TU5**), the organic content determined by this method was 0.0922 g per 0.20 g of nanomaterial (ca. 46.1 wt.%).

Ligand exchange procedures

Ligand exchange with 2-mercaptopropionic acid (2-MPA). In a three-neck flask, dry methanol (300 ml) and 2-MPA (4 ml) were combined and degassed by bubbling argon for 15 minutes. Then, under continuous stirring at room temperature, a solution of tetramethylammonium hydroxide (TMAH, 25% in methanol) was added dropwise until the pH reached 10 (approximately 25 ml). The mixture was stirred for 1 h under argon, after which ZnS QDs (1 g) were added. Stirring continued until full homogenization was achieved (approximately 3 hours). The volume of solution was reduced to 100 ml by evaporation under reduced pressure using a rotary evaporator. The resulting water-soluble QDs were precipitated by the slow addition of ethyl acetate (500 ml), isolated by centrifugation (6,000 rpm, 5 min), decanted, and dried in a vacuum oven at 50 °C for 3 h. The mass of the ligand-exchanged ZnS QDs was recorded (0.49 g).

Ligand exchange with phosphate-functionalized methacrylates. ZnS QDs (500 mg) obtained from the large-scale synthesis, with previously determined ligand content, were dispersed in 10 ml of chloroform. The calculated amount (0.2385 g) of BMEP was added to the colloidal solution at room temperature under an argon atmosphere. The mixture was stirred for 3 h to allow ligand exchange. After this period, the solvent was reduced to a total volume of ∼2 ml using a rotary evaporator and diluted with 20 ml of hexane. The resulting precipitate was isolated by centrifugation at 6,000 rpm for 5 min and dried under vacuum without heating. The mass of the purified ligand-exchanged QDs was 0.35 g. An analogous procedure was employed for the second ligand exchange using a molar equivalent (0.2385 g) of PODM instead of BMEP. After isolation and drying, the final product mass was 0.22 g.

Film preparation and polymer embedding

Thin films of both pristine ZnS QDs and polymer-embedded nanocomposites were prepared using static spin-coating. Standard soda-lime microscope glass slides (25 × 25 mm) were used as substrates. The slides were cleaned by sonication in water with detergent, thoroughly rinsed with distilled water and isopropyl alcohol, and dried using compressed air. Before deposition, the substrates were washed with chloroform and dried again.

- For the preparation of pure QDs films, ZnS QDs (100 mg) were dispersed in chloroform (or in methanol in the case of 2-MPA-capped QDs) and deposited by spin-coating at 500 rpm for 5 s, followed by 3000 rpm for 20 s.

Two approaches were used for incorporating ZnS QDs into a polymer matrix:

- Physical dispersion in polymer solution:

ZnS QDs (25 mg) were added to a solution of PMMA or PVK (500 mg in 5 ml of chloroform) and mixed until homogeneously dispersed. In the case of 2-MPA-capped ZnS QDs, dispersion was performed in a solution of PEG (Mn 6,000; 500 mg in 5 ml of methanol). The resulting mixtures were spin-coated onto glass slides using the same protocol.

- In situ copolymerization with polymerizable ligands:

QDs capped with methacrylate-functionalized ligands (PODM or BMEP) were directly incorporated into a polymer matrix via radical copolymerization. Vinyl carbazole (1500 mg) or methyl methacrylate (1500 mg), ZnS QDs (75 mg), AIBN (35 mg), and xylene (8 ml) were combined in a sealed flask and heated to 75 °C for 5 days under an argon atmosphere. After polymerization, the mixture was transferred into xylene and slowly precipitated into 100 ml of hexane. The resulting copolymer was collected by filtration (glass frit S2), washed with hexane, and dried under vacuum. Thus, we successfully prepared copolymers of PVK with ZnS QDs capped by PODM ligand (PVK-*co*-ZnS) and PMMA with ZnS QDs capped by BMEP ligand (PMMA-*co*-ZnS). The dried copolymers (200 mg) were

then redissolved in chloroform (2 ml) and spin-coated under the same conditions as physical dispersions.

Characterization techniques

Structural and spectroscopic characterization was performed using a combination of NMR, FTIR, XRD, XPS, electron microscopy, AFM, and optical spectroscopy techniques. Solution-phase nuclear magnetic resonance (NMR) spectra were recorded in $CDCl_3$ at 295 K on a Bruker Ascend 500 MHz spectrometer equipped with a Prodigy cryoprobe and a z-gradient system. Samples (20-40 mg) were dissolved in 0.5 ml of the deuterated solvent. Proton and carbon chemical shifts were calibrated using residual solvent signals (δ = 7.26 ppm for ^{1}H and 77.23 ppm for ^{13}C) and are reported in parts per million (ppm).

Fourier-transform infrared (FTIR) spectra were collected using a Bruker Vertex 70V instrument with a diamond ATR unit, over the 3500-200 cm^{-1} range at a resolution of 2 cm^{-1}. Powder X-ray diffraction (XRD) patterns were acquired on a PANalytical EMPYREAN diffractometer (Cu Kα radiation, λ = 1.5418 Å) over a 2θ range of 20-70° with a step size of 0.05°. Electron microscopy was employed for analysis of morphology and composition. Scanning transmission electron microscopy (STEM) and energy-dispersive X-ray spectroscopy (EDS) were performed on a Tescan LYRA 3 microscope equipped with an Aztec X-Max 20 detector (Oxford Instruments), operated at 20 (EDS) or 30 kV (STEM). Solutions of QDs in $CHCl_3$ were drop-cast onto a TEM 400 mesh copper grid with an electron-transparent membrane from amorphous carbon (Ted Pella, Inc.). Atomic force microscopy (AFM) was used to evaluate the topography of thin films. Measurements were performed in semi-contact mode on an NTEGRA (NT-MDT) instrument using NSG 10 silicon tips. Images were acquired over 20 × 20 µm2 areas, and height distributions were analysed from the corresponding histograms.

The surface chemical composition was evaluated by X-ray photoelectron spectroscopy at room temperature (XPS, ESCA 2SR, Scienta Omicron) using a monochromatic Al Kα (1486.7 eV) X-ray source. The X-ray source was operated at 200 W. The binding energy scale was referenced to adventitious carbon (284.8 eV). CasaXPS software (Casa software Ltd) was used to analyse the spectra.

Optical measurements included UV-Vis and photoluminescence (PL) spectroscopy. Absorbance spectra were obtained on a Shimadzu UV-3600 spectrophotometer over the 200-700 nm range. PL spectra were recorded using a PTI QuantaMaster 400 fluorometer, with excitation wavelengths ranging from 250 to 500 nm. To monitor the reaction progress, aliquots (30 µl) were taken from the reaction mixture at specified reaction times (20 sec, 1 min, 2 min, 5 min, 10 min, 25 min, and after the reaction mixture had cooled. Aliquots were subsequently dispersed in 1.5 ml of $CHCl_3$ and characterized by the specified techniques. The resulting QDs samples were also dispersed in $CHCl_3$, with the solution concentration ranging from 1 to 0.01 wt.%. The prepared thin films were analysed without further modification in the same spectral range as the solutions, for direct comparison of optical properties. The lifetime measurements of ZnS QDs solutions capped by various ligands were also performed on a PTI QuantaMaster 400 fluorometer using a 310 nm laser diode as a light source.

Results and discussion

Scalable synthesis and ligand exchange

The synthesis of ZnS QDs via hot-injection of substituted thioureas into zinc linoleate precursor systems (Figure 1) follows a classical nucleation-growth mechanism consistent with LaMer-type behaviour.[17] Upon injection at elevated temperature (240 °C), the rapid decomposition of thiourea provides an immediate supply of sulphide ions, leading to a burst of homogeneous nucleation.[18] The presence of coordinating solvents (ODE, OAm) and long-chain organic acids modulates the surface energy of the forming nuclei and helps stabilize small crystalline domains. Following nucleation, nanocrystal growth proceeds under diffusion-controlled conditions, with the preformed zinc-linoleate complex and substituted thiourea acting as a relatively slow donor of Zn^{2+} and S^{2-} ions. The choice of substituted thiourea influences both the decomposition rate and the local coordination environment during nanocrystal nucleation and early growth due to variable steric and electronic effects. This tunability offers an additional lever to adjust particle size and surface coverage. Notably, the high boiling point of ODE and the absence of polar solvents prevent premature aggregation, allowing for controlled growth over the 25-minute reaction window. The reproducibility and yield of the synthetic protocol, including successful upscaling to multigram quantities, indicate the robustness of the precursor conversion and surface stabilization strategy.

ARTICLE

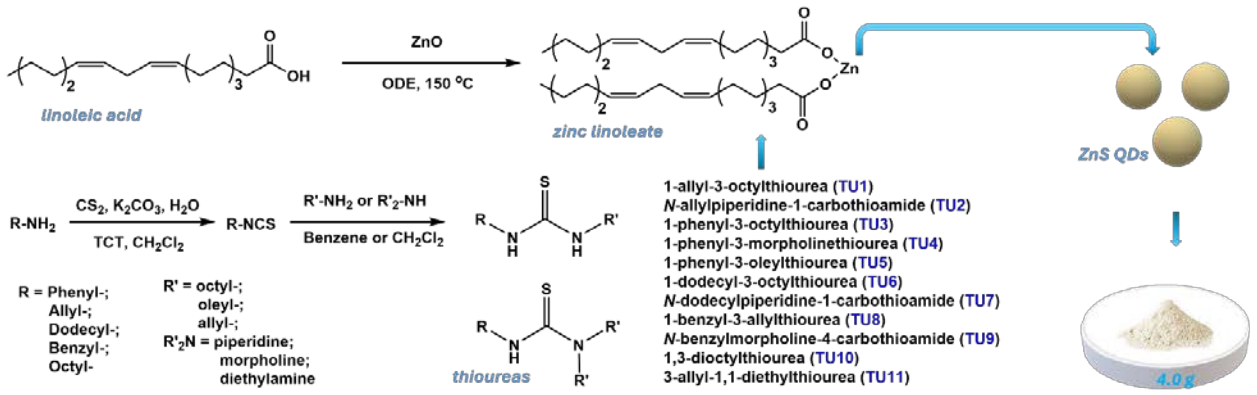

Figure 1. Schematic overview of ZnS QDs synthesis using substituted thioureas.

The high organic content (~46 wt.%) of as-synthesized ZnS QDs offers a versatile platform for post-synthetic ligand exchange. The native ligands, formed in situ during thiourea decomposition and coordination with linoleate, are efficiently displaced by more functional ligands under mild conditions. The success of this exchange was confirmed by complete phase transfer and recovery of stable solid products after centrifugation. 2-Mercaptopropionic acid was employed to introduce hydrophilic carboxylate and thiol groups, enabling dispersion in polar solvents and aqueous media. The two phosphate-functionalized methacrylates, BMEP and PODM, provided anchoring groups for covalent embedding into polymer matrices via radical copolymerization. This strategy not only ensures compatibility with acrylate-based hosts (*e.g.*, PMMA, PVK) but also allows fine-tuning of QDs distribution and mobility within the polymer. Ultrasonic processing in nonpolar solvents (hexane) facilitated ligand exchange without significant aggregation, and vacuum drying preserved the nanocrystal integrity. The recovered masses of exchanged QDs were consistent with partial retention of organic content, and further characterization confirmed successful surface modification.

Structural and morphological characterization

STEM images were collected to evaluate the size and shape of the prepared QDs. The prepared samples were measured by drop-casting a solution of QDs onto a TEM copper grid with an electron-transparent membrane made from amorphous carbon. Although the low contrast of ZnS QDs makes precise size determination challenging, approximate particle dimensions were estimated using *ImageJ* software and are also presented in Figure 2. To enhance the statistical reliability of the analysis, several regions across each TEM grid were examined, and particle size distributions were derived from measurements of multiple individual nanocrystals per sample. All samples exhibit well-dispersed, nearly spherical QDs with narrow size distributions. Notably, despite the wide structural diversity of the thioureas employed during synthesis, including short-chain aliphatic, bulky aromatic, and disubstituted variants, the resulting ZnS QDs exhibit highly uniform particle sizes, typically ranging from approximately 6.2 to 6.8 nm. A slight increase in average size was observed only in the samples synthesized using **TU4** and **TU8**, with particle diameters of approximately 7.5 and 7.9 nm, respectively. Importantly, no clear correlation was found between the nature of the substituents in the thiourea molecules and the final QD size. For instance, ZnS QDs synthesized using **TU2** and **TU6**, which differ significantly in molecular geometry and substituent bulkiness, yielded nearly identical particle sizes.

These findings suggest that other parameters, such as precursor solubility in the reaction medium, the rate of thiourea decomposition, and the kinetics of nucleation from zinc linoleate intermediates, may play a more significant role in determining particle dimensions. Furthermore, the comparison between standard and large-scale synthesis using **TU5** revealed no significant morphological differences, indicating that the method is scalable without compromising size uniformity or quality. This supports the reproducibility and robustness of the developed synthetic approach for preparing ZnS QDs with tunable surface properties.

The powder XRD patterns of the synthesized ZnS QDs were measured to confirm their crystalline structure. The XRD patterns and lattice parameters of ZnS QDs synthesized from various substituted thioureas are presented in Figure S1 and Table S1 in the Supplementary Materials.

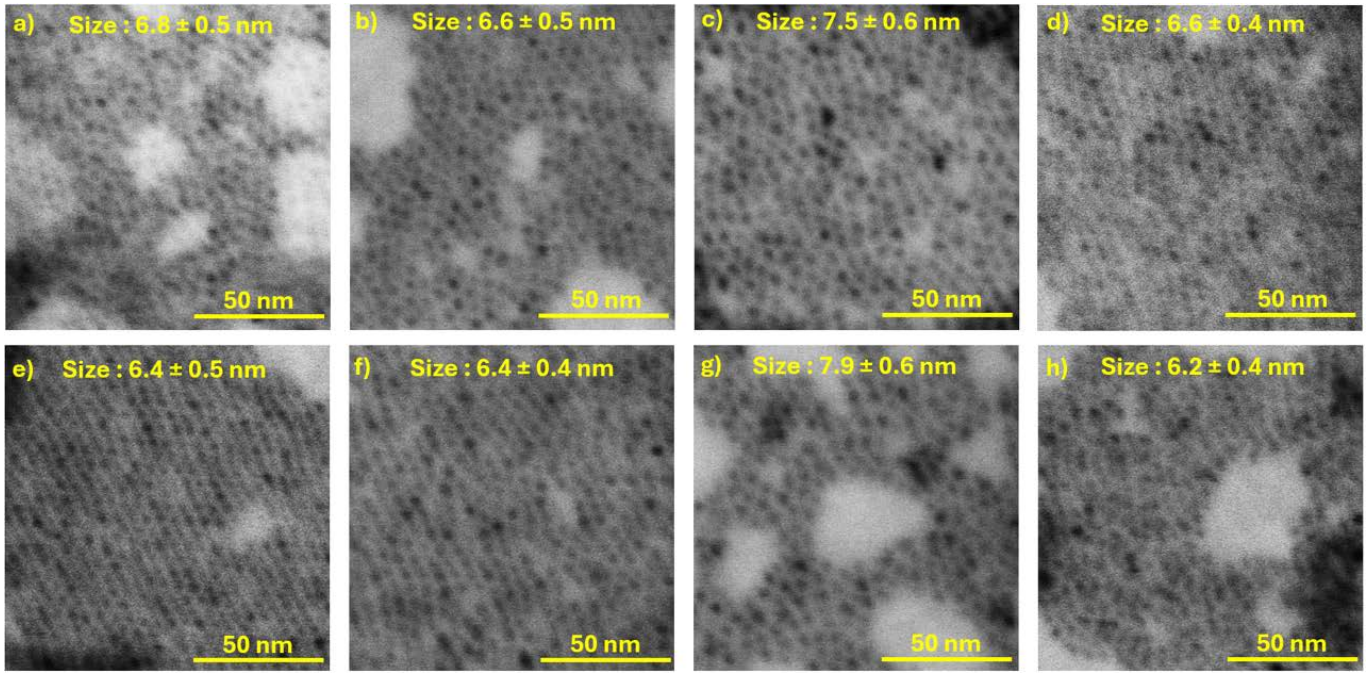

Figure 2. STEM images of ZnS QDs prepared by the hot-injection technique from substituted thioureas - a) **TU1**, b) **TU2**, c) **TU4**, d) **TU5**, e) **TU6**, f) **TU7**, g) **TU8**, h) **TU5** (large-scale synthesis), and estimated size of QDs.

All XRD patterns exhibit 3 main peaks at 2θ = 29.1, 48.2, and 57.0°, which can be assigned to the (111), (220), and (311) crystallographic planes of a cubic ZnS structure (ref. 98-067-1466) with the space group F-43*m*. No significant changes in the crystalline structure were observed for ZnS QDs synthesized using different thioureas, and only minor changes in lattice parameters (presented in *Supplementary Materials* - Table S1). XRD patterns of ZnS QDs after the ligand exchange (Figure 3) were also measured to confirm the preservation of lattice parameters and to rule out any crystal fragmentation during the ligand exchange process with the capping agents 2-MPA, BMEP, and PODM.

The cubic structure of the ZnS QDs remains unchanged, consistent with the expected zinc blende structure, with three main peaks at 2θ = 29.1, 48.2, and 57.0°. The XRD pattern of ZnS QDs after ligand exchange with PODM displays a distinct shift of the (111), (220), and (311) reflections toward lower 2θ values, indicating a slight expansion of the crystal lattice. This shift is not observed for ZnS QDs capped with 2-MPA or BMEP, whose diffraction peak positions remain essentially unchanged relative to the LA-capped reference, suggesting a unique structural effect induced by PODM. The lattice expansion can be attributed to partial extraction of surface Zn^{2+} ions via strong chelation by the phosphonate headgroup, which alters the local stoichiometry and weakens lattice cohesion near the surface. As a result, the unit cell expands slightly, producing a detectable shift in the diffraction peaks. Such ligand-induced modifications of crystal structure have been previously reported for phosphonate- and phosphate-based ligands, which are known to chelate surface metal ions and alter the coordination environment, sometimes leading to measurable changes in unit cell dimensions.[19,20] Notably, this structural perturbation does not stem from oxidation or degradation processes. The slight decrease in the lattice parameter observed after ligand exchange with 2-MPA and BMEP is within the range of instrumental variation and does not indicate structural alteration of the ZnS core.

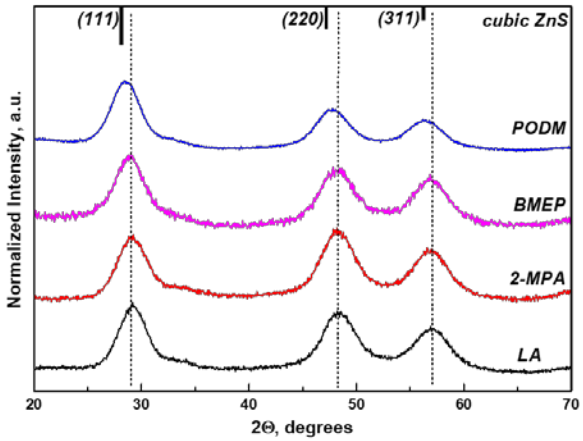

Figure 3. XRD patterns of ZnS QDs synthesized by the hot-injection method from **TU5**, before and after the change of capping ligand.

The EDS spectra of ZnS QDs before and after the capping ligand exchange were also gathered to study the changes in composition induced by the exchange. The elemental compositions of QDs with various capping ligands are presented in Table 1. The QDs capped with LA show a higher apparent Zn content due to the presence of stabilizing zinc linoleate species on the surface. After ligand exchange with 2-MPA, an increase in S and C signals was detected, consistent with the introduction of a sulfur-containing ligand. In contrast, QDs capped with PODM and BMEP exhibit no substantial change in Zn and S content but display elevated O levels and clearly detectable P signals, both originating from the phosphonate-based ligands. These elemental variations match the expected composition of the respective capping ligands and therefore support the successful completion of the ligand-exchange process.

ZnS QDs surface analysis

A detailed surface characterization was performed to investigate how ligand exchange modifies the chemical environment, coordination modes, and surface composition of the ZnS QDs without altering the crystalline ZnS core. Given the high surface-to-volume ratio of 6-8 nm particles and the presence of a substantial organic shell originating from zinc linoleate, even partial ligand substitution can induce measurable changes in vibrational signatures, elemental composition, and binding motifs. To preserve the dispersibility of the nanocrystals, only partial rather than complete replacement of linoleate with methacrylate-based phosphorus-containing ligands was performed. Therefore, surface-sensitive techniques, including FTIR, XPS, and complementary EDS analysis, were employed to confirm the successful replacement of linoleate by 2-MPA, BMEP, and PODM, and to elucidate the specific coordination modes for each ligand.

The ATR spectra of the ZnS QDs are shown in Figure 4. To monitor ligand exchange, all spectra were normalized to the maximum intensity of the band in the 400-200 cm^{-1} region, whose maximum corresponds to the transverse optical (TO) phonon mode of cubic ZnS. For comparison, the spectra of the pure ligands 2-MPA, BMEP, and PODM are also included. The ATR spectrum of the LA-capped ZnS QDs is characterized by absorption bands assignable to linoleyl group: 3008 cm^{-1} (ν C-H in -CH=CH-), 2960 cm^{-1} (ν_{as} CH_3), 2922 cm^{-1} (ν_{as} CH_2), and 2852 cm^{-1} (ν_s CH_2).

Table 1 Elemental composition of prepared ZnS QDs before and after capping ligand exchange.

Ligand	Zn (at. %)	S (at. %)	C (at. %)	O (at. %)	P (at. %)
LA (TU5)	9.6 ± 0.4	5.9 ± 1.0	75.4 ± 0.7	9.1 ± 0.7	0.0 ± 0.0
2-MPA	16.1 ± 0.6	16.4 ± 0.6	54.9 ± 1.8	12.6 ± 0.8	0.0 ± 0.0
BMEP	10.9 ± 0.2	7.0 ± 0.3	52.1 ± 0.7	27.1 ± 0.6	2.9 ± 0.2
PODM	9.8 ± 0.4	6.4 ± 0.8	62.8 ± 1.0	18.4 ± 0.9	2.6 ± 0.3

The band at 1544 cm^{-1} and the broad feature between 1480 and 1340 cm^{-1} correspond to the asymmetric and symmetric stretching vibrations of the carboxylate group.[21,22] These characteristic vibrations confirm the presence of zinc linoleate as the native capping ligand.

After ligand exchange with BMEP, the intensity of LA-related vibrations decreases significantly. New absorptions appear at 1717 cm^{-1} (ester C=O), 1637 cm^{-1} (vinyl C=C), 1323 and 1297 cm^{-1} (C-O stretching with contributions from P=O), along with multiple bands in the 1300-900 cm^{-1} region associated with P=O and P-O vibrations of the phosphate group. Compared to pure BMEP, the P-OH band at 2300-2200 cm^{-1} disappears, the band at 983 cm^{-1} decreases, and a stronger band emerges at ~1067 cm^{-1}, consistent with partial ion-exchange of BMEP and the formation of surface P-O-Zn linkages through coordination of the deprotonated phosphate group.[23,24] These changes confirm the partial replacement of LA by BMEP on the ZnS surface. The PODM-capped ZnS QDs show a similar decrease in LA vibrations together with new features characteristic of methacrylate and phosphonate groups. The disappearance of the P-OH band (2300-2200 cm^{-1}), reduction of the 952 cm^{-1} band, and emergence of a strong band near 1066 cm^{-1} are consistent with partial ion-exchange of PODM and the formation of surface P-O-Zn linkages through coordination of the deprotonated phosphonate group.

After the exchange with 2-MPA, LA-related vibrations disappear completely. The absence of the S-H stretching band at 2555 cm^{-1} indicates thiol deprotonation and formation of S-Zn surface bonds. Bands at 1559 and 1384 cm^{-1} correspond to the asymmetric and symmetric stretching of the carboxylate (COO^-) group of 2-MPA, bonded with TMAH. Broad bands at 3365 and 1645 cm^{-1} arise from adsorbed water, commonly observed for hydrophilic, carboxylate-terminated ligands. A band at ~949 cm^{-1} corresponds to C-N vibrations of residual TMA^+ ions from the exchange medium.[23-25] Overall, the spectral features confirm effective replacement of LA by 2-MPA and binding through the thiolate group.

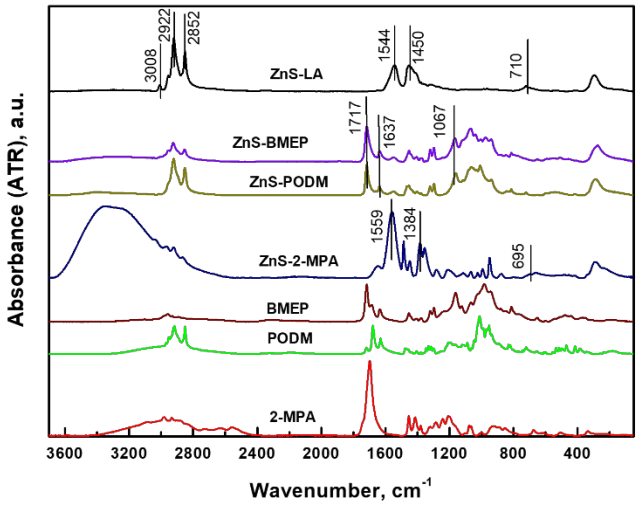

Figure 4. FTIR (ATR) spectra of ZnS QDs before and after ligand exchange. The ligands BMEP, PODM and 2-MPA are included for comparison.

X-ray photoelectron spectroscopy (XPS) was employed to confirm the chemical integrity of the ZnS QDs surface and to evaluate the success of ligand exchange with phosphonate-based ligands. The survey spectra (Figure 5a) exhibit the presence of Zn, S, C, and O in all four samples, while distinct P 2*p* signals are observed exclusively in BMEP- and PODM-capped ZnS QDs (Figure 5d), confirming the attachment of phosphorus-containing ligands.

High-resolution Zn 2*p* spectrum (Figure 5b) reveal characteristic doublets at ~1021.8 eV (Zn $2p_{3/2}$) and ~1044.8 eV (Zn $2p_{1/2}$), consistent with Zn^{2+} in the ZnS lattice. Importantly, no energy shifts, satellite features, or discernible signals from oxidized Zn species are detected, indicating that the ZnS core remains chemically unaltered during the ligand exchange process. Similarly, the S 2*p* region (Figure 5c) demonstrates a main doublet at ~161.7 and ~163.0 eV, corresponding to S^{2-} bound to zinc.[26,27] The absence of higher binding energy peaks indicates that no oxidized sulfur species are present within the detection limit. The P 2*p* core level spectrum of the PODM-functionalized sample (Figure 5e) exhibits a doublet centred at ~133.5-134.3 eV, which can be deconvoluted into components consistent with P=O and/or P-O-Zn environments.[28,29] This suggests that the phosphonate groups not only remain intact but also form coordination interactions with surface zinc atoms, most likely through Zn-O-P linkages. Rather, they are attributed to surface reconstruction or lattice relaxation induced by phosphonate coordination, possibly accompanied by partial rearrangement of surface zinc ions. Similar phenomena have been reported for other phosphonate-functionalized metal chalcogenide nanostructures.

Optical properties in solution and films

Optical characterization of ZnS QDs provides a direct probe of their electronic band structure and surface passivation efficiency. Since the optical response of II-VI semiconductor nanocrystals is strongly governed by the surface coordination environment, ligand exchange with carboxylate (2-MPA) and phosphonate ligands (BMEP, PODM) was expected to influence both the band-edge absorbance and defect-related emission pathways. UV-Vis, photoluminescence (PL), and photoluminescence excitation (PLE) spectra were therefore recorded to elucidate the correlations between surface chemistry, energy gap modulation, and photophysical stability. The progress of ZnS nanocrystal formation was monitored by collecting aliquots from the reaction mixture at defined time intervals. Both the absorbance and emission spectra of the aliquots (Figure 6) exhibit a continuous increase in intensity, confirming the rapid nucleation and growth of ZnS QDs during the early stages of synthesis. The progressive red shift of both absorbance and PL maxima within the first 10 minutes reflects particle growth and an increase in the number of optically detectable nanocrystals. After this period, no further shift in the spectral peak positions is observed, indicating that the particle size has become stabilized, and the growth process has reached completion.[30,31]

ARTICLE

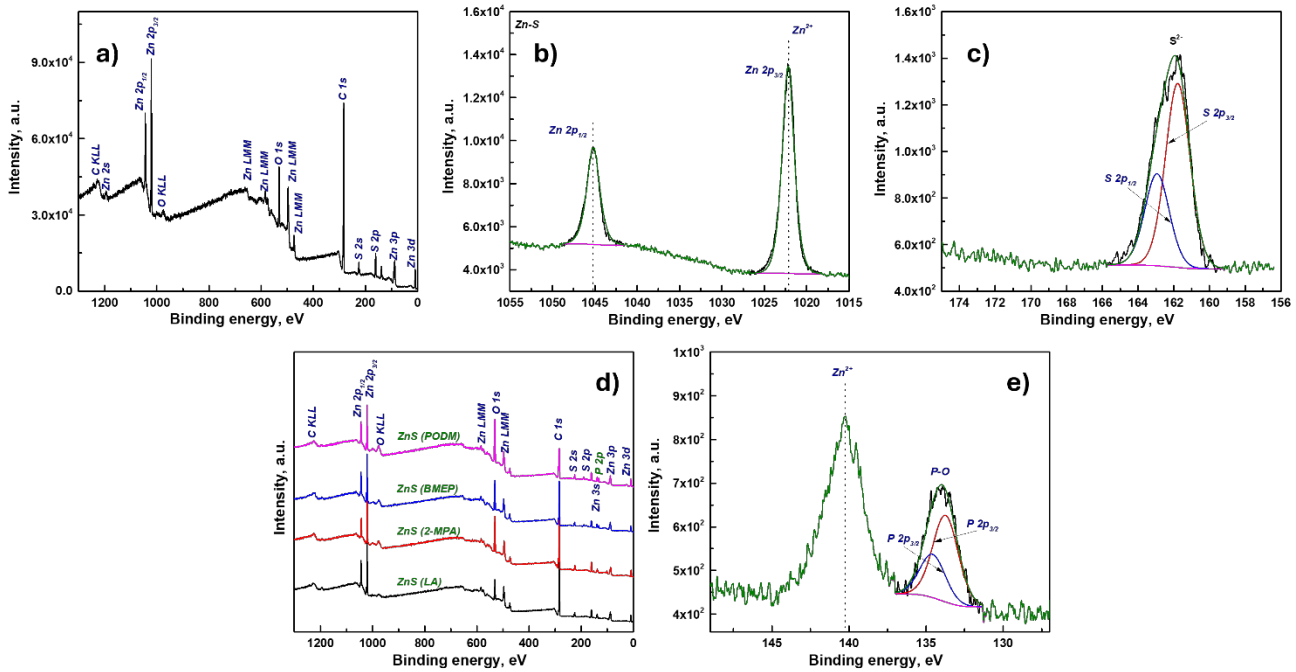

Figure 5. XPS survey spectra of ZnS QDs with different surface ligands: (a) full survey scan of ZnS QDs obtained via large-scale synthesis; (b) Zn 2p spectrum; (c) S 2p spectrum; (d) stacked survey spectra for ZnS QDs with LA, 2-MPA, BMEP, and PODM ligands; (e) P 2p spectrum of PODM-functionalized ZnS QDs

The absorbance and photoluminescence spectra of ZnS quantum dots (Figure 7) demonstrate a clear dependence of their optical characteristics on the properties of the resulting ZnS QDs rather than on the molecular structure of the precursor. All samples display a broad absorbance band between 250 and 350 nm, typical of direct electronic transitions in ZnS nanocrystals. The weak and only partially resolved first excitonic feature can be attributed to a moderate size dispersion and the contribution of surface-related states. The absorbance maxima range from 306 nm (**TU5**, **TU6**) to 326 nm (**TU4**, **TU8**), indicating small variations in the average particle size of the ZnS QDs. The detailed ABS and PL spectra of all synthesized QDs are presented in the *Supplementary Materials* (Figures S2 and S3). The absorption spectrum of the cooled aliquot is presented for general reference only, since quantitative comparison with hot aliquots is limited by temperature-dependent viscosity effects that lead to unavoidable differences in effective concentration.

The observed red shifts of both absorbance and emission bands for ZnS (**TU4**) (λ_{ABS} = 326 nm, λ_{PL} = 438 nm) and ZnS (**TU8**) (λ_{ABS} = 326 nm, λ_{PL} = 442 nm) correspond to larger ZnS nanocrystals with weaker quantum confinement and lower optical band-gap energies (3.58 eV and 3.55 eV, respectively). Conversely, **TU5** and **TU6** show the shortest absorbance wavelengths (306 nm) and the highest band-gap energies (3.77 eV and 3.73 eV), characteristic of smaller nanocrystals with stronger confinement. Intermediate samples ZnS (**TU1**, T**U2**, **TU7**) exhibit λ_{ABS} = 316-319 nm and λ_{PL} = 434 nm, consistent with moderately sized ZnS QDs.

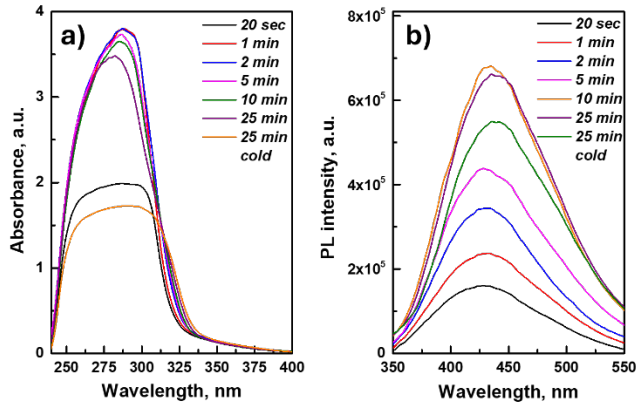

Figure 6. UV-Vis absorbance (a) and photoluminescence (b) spectra of ZnS QDs growth (from large-scale synthesis using **TU5**).

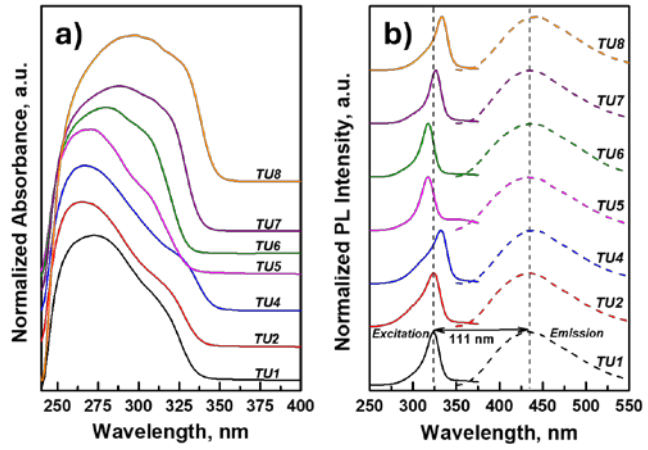

Figure 7. Normalized UV-Vis absorbance (a) and photoluminescence (b) spectra of ZnS QDs synthesized using various substituted thioureas as a precursor (**TU1**-**TU8**).

The Stokes shift, calculated as the difference between excitation and emission maxima, ranges from 106 nm to 120 nm (Table 2). The largest Stokes shift (120 nm) is observed for **TU5**, suggesting stronger exciton relaxation through surface or defect-related states. The smallest shifts are observed for ZnS (**TU4**, 106 nm) and ZnS (**TU8**, 109 nm), in agreement with their larger particle sizes and weaker confinement effects.

The optical band-gap values (E_g = 3.55-3.77 eV) follow the expected size-dependent trend, decreasing with increasing particle size. Assuming the ZnS QDs are a direct band semiconductor, the band gap value can be calculated from the spectral dependence of the absorbance coefficient using the Tauc formula.[32]

$$(\alpha h\nu) \sim \left(h\nu - E_g\right)^{1/2}$$

This equation enables the determination of a material's band gap from its experimental absorbance spectra.

Table 2 Optical properties of ZnS QDs synthesized from various substituted thioureas. Peak maximum of the first exciton in absorbance spectra (λ_{ABS}), peak maximum of the excitation λ_{EXC}, and emission λ_{PL} spectra, Stokes shift, and band gap (E_g).

Substituted thioureas	λ_{ABS}, nm	λ_{EXC}, nm	λ_{PL}, nm	Stokes shift, nm	E_g, eV
TU1	316	323	434	111	3.69
TU2	317	323	434	111	3.66
TU4	326	332	438	106	3.58
TU5	306	318	432	114	3.77
TU6	306	318	438	120	3.73
TU7	319	326	434	108	3.63
TU8	326	333	442	109	3.55
TU5 Large-scale	308	319	432	113	3.71

To achieve this, plots of $(\alpha h\nu)^2$ versus $h\nu$ were generated for all the studied ZnS QDs, and the band gap energies (E_g) were estimated through linear extrapolation. The obtained E_g values are close to those of bulk ZnS (3.61 eV)[33] and are presented in Table 2. Due to the quantum confinement effect, smaller QDs (e.g., those synthesized from **TU5** and **TU6**) exhibit larger band gaps than bulk ZnS, while larger QDs (e.g., synthesized from **TU4** and **TU8**) have band gaps that approach the bulk value. The ZnS QDs (**TU5**), prepared by large-scale synthesis (λ_{ABS} = 308 nm, E_g = 3.71 eV), exhibit nearly identical spectral parameters to the small-scale batch, confirming the reproducibility and scalability of ZnS QD synthesis. Overall, these data demonstrate that controlled modification of precursor composition allows fine-tuning of ZnS QDs size, emission wavelength, and exciton relaxation dynamics without altering the chemical composition of the ZnS core.

The differences in optical properties between the ZnS QDs prepared by small-scale (standard) and large-scale syntheses were studied using the gathered UV-Vis ABS, PL, and PLE spectra. The direct comparison of the obtained spectra is presented in Figure 8, which demonstrates that the positions of the first exciton, excitation peak, and emission peak are nearly identical.

Beyond the intrinsic size-dependent behaviour, the ZnS QDs investigated here provide a rare opportunity to examine how three fundamentally different classes of surface ligands, lipophilic long-chain carboxylates (LA), compact hydrophilic bifunctional ligands (2-MPA), and amphiphilic, vinyl-functionalized phosphorus-based ligands (BMEP and PODM), reshape exciton relaxation pathways and defect passivation.[34] Such a direct comparison between lipophilic, hydrophilic, and reactive amphiphilic ligand environments (Figure 9) is uncommon for ZnS nanocrystals and enables a deeper understanding of how ligand architecture governs photoluminescence efficiency, stability, and potential integration into polymer matrices.

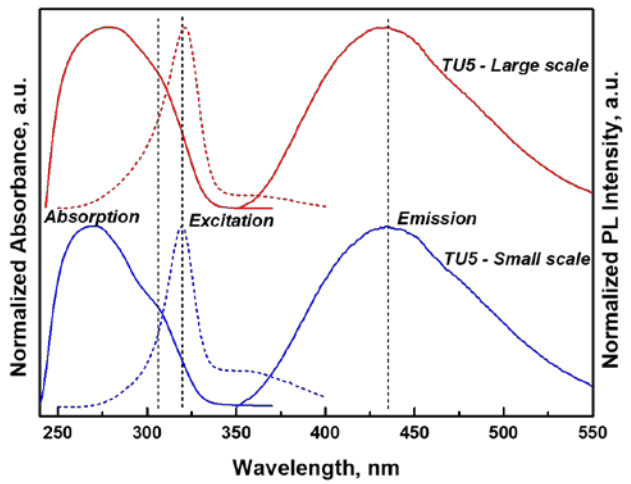

Figure 8. Comparison of UV-Vis absorbance and PL spectra of ZnS QDs synthesized from TU5 by standard and large-scale synthesis.

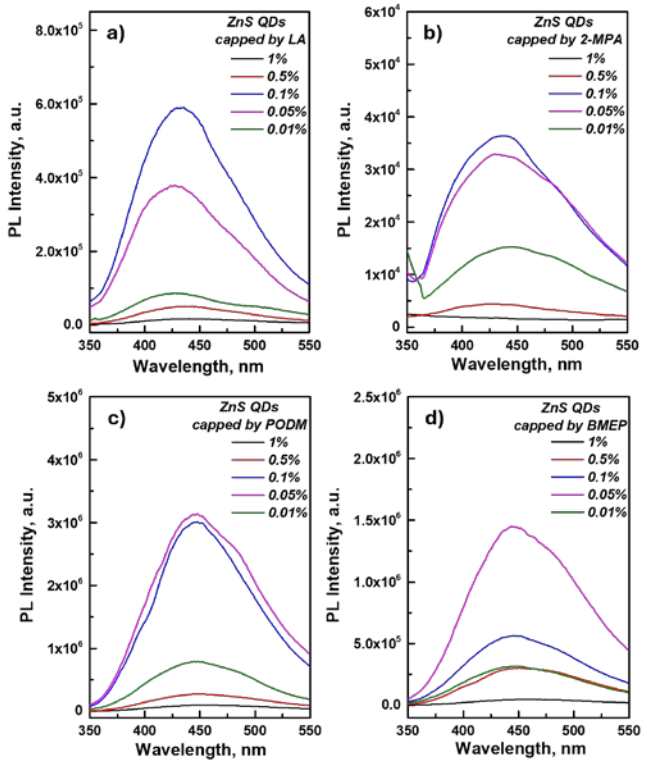

Figure 9. Photoluminescence (PL) spectra of ZnS QDs synthesized from **TU5** with different stabilizing ligands: a) LA, b) 2-MPA, c) PODM, d) BMEP.

To further understand the influence of surface passivation, ZnS QDs obtained from the **TU5** precursor were subjected to ligand exchange with several coordinating ligands. As illustrated in Figure 9, the ligand environment exerts a decisive influence on the photoluminescence response of the ZnS QDs, reflecting differences in surface passivation strength and defect suppression. Replacing LA with 2-MPA results in a significant decrease in PL intensity (from 5×10^5 to 4×10^4), while the positions of the excitonic, excitation, and emission bands remain unchanged (Figure 10, Table 3).[35]

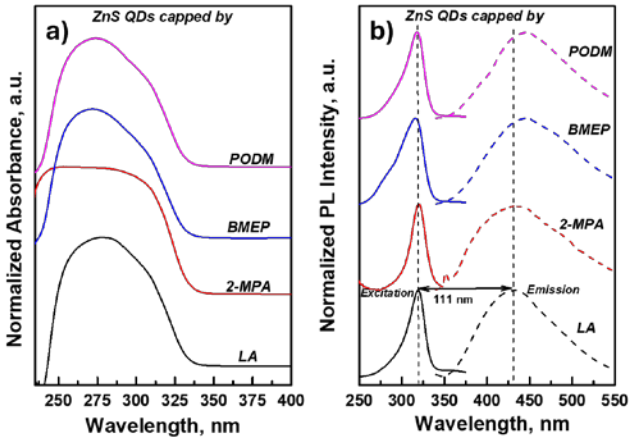

Figure 10. UV-Vis absorbance (a) and PL (b) spectra of ZnS QDs with different capping ligands LA, 2-MPA, BMEP, and PODM.

In contrast, ligands bearing longer hydrocarbon fragments, such as LA, PODM, and BMEP, provide a more complete passivation of surface trap states, which translates into markedly enhanced PL intensities and improved optical stability.[36] Upon exchange to BMEP or PODM, the PL output increases to 1.5×10^6 and 3×10^6, respectively (Figure 9). These samples also exhibit a slight blue shift in the excitation maximum coupled with a red shift in the PL emission, leading to an increased Stokes shift (Figure 10, Table 3). Taken together, these variations in PL behaviour reflect ligand-dependent modulation of surface defect density, with some ligands suppressing non-radiative, defect-mediated processes more effectively than others.

Photoluminescence decay kinetics were measured for ZnS QDs synthesized from the **TU5** precursor and subsequently capped with different ligands, using pulsed excitation at 310 nm while monitoring emission at λ_{PL} to resolve exciton recombination dynamics. The decay profiles were fitted with a single-exponential model deconvoluted with the instrument response function (IRF, measured using an aqueous LUDOX standard). Attempts to apply multi-exponential fits to the PODM- and BMEP-capped QDs produced unphysical parameters (negative or oppositely signed amplitudes), justifying the use of a simplified single-component model. For comparison, LA- and 2-MPA-capped samples were analysed using both single- and two-exponential fits (Table 3).

The PL decay traces of LA- and 2-MPA-capped QDs reveal two well-defined components: a dominant, fast component (19.17 ns and 2.51 ns, respectively), corresponding to non-radiative exciton relaxation via surface traps, and a weaker, longer-lived component (136.92 ns and 20.52 ns), associated with intrinsic radiative recombination of the ZnS core.[15]

Table 3 Optical properties of synthesized ZnS QDs with different stabilizing ligands. Peak maximum of the first exciton in absorbance spectra (λ_{ABS}), peak maximum of the excitation λ_{EXC}, and emission λPL spectra, Stokes shift, band gap (E_g), and fitting results of the PL decay curves (τ and A) using one-exponential and two-exponential fits.

Optical parameters	LA	2-MPA	BMEP	PODM
λ_{ABS}, nm	308	310	308	308
λ_{EXC}, nm	319	320	315	318
λ_{PL}, nm	432	433	444	446
Stokes shift, nm	113	113	129	128
E_g, eV	3.81	3.77	3.83	3.82
τ, ns (1 exp.)	85.29	11.79	250.38	168.17
A (1 exp.)	0.0815	0.1995	0.1222	0.0920
τ_1, ns (2 exp.)	19.17	2.51	250.24	167.85
τ_2, ns (2 exp.)	136.92	20.52	250.23	167.84
A_1 (2 exp.)	0.1880	0.6908	1.0875	4.4964
A_2 (2 exp.)	0.0405	0.0694	-0.9652	-4.3997

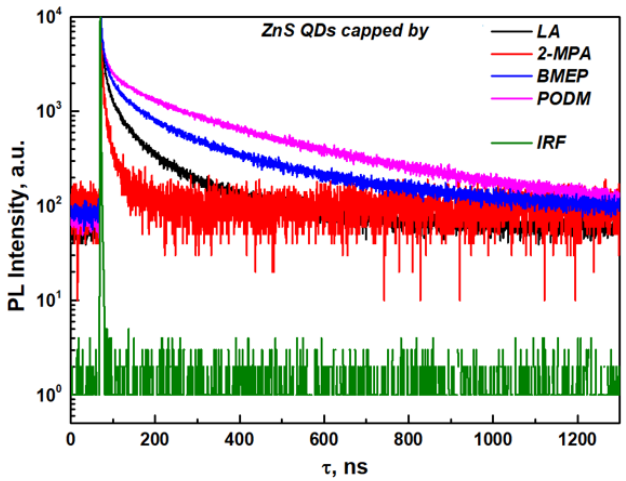

Figure 11. PL decay kinetic curves for ZnS QDs capped by different ligands.

In contrast, QDs capped with BMEP or PODM show no detectable fast component, consistent with reduced surface defect densities and the enhanced PL efficiencies described above. While ligand exchange significantly modifies non-radiative recombination pathways and thus affects the PL lifetime, the steady-state emission spectra remain largely unchanged because the dominant emissive states of ZnS QDs are energetically preserved. As a result, kinetic changes in excited-state decay can occur without noticeable shifts in the PL spectral shape.

Integration into polymers and film formation

The integration of ZnS QDs into polymer matrices represents a crucial step toward translating their intrinsic optical properties into functional, processable materials. While colloidal ZnS QDs exhibit excellent stability and high luminescence in solution, their direct application in devices requires uniform, adherent, and optically detectable thin films. However, aggregation, poor interfacial compatibility, and ligand desorption often limit film quality and long-term stability. The ligand-engineering strategy developed in this work overcomes these challenges by enabling both physical and chemical routes to polymer incorporation. Hydrophobic and hydrophilic surface terminations were chosen to ensure compatibility with different polymer hosts, while phosphonate-based methacrylate ligands provide reactive sites for covalent anchoring within polymer chains. This dual approach allows precise control over the QDs-polymer interface, preserving the structural integrity and emission efficiency of ZnS nanocrystals.[37] To investigate the difference between the two approaches, thin films without polymer were also prepared from QDs capped with LA and 2-MPA.

The resulting nanocomposite systems not only exhibit uniform photoluminescent films but also demonstrate enhanced environmental robustness compared with neat ZnS QDs films. The polymer encapsulation effectively suppresses QD aggregation and protects the surface from oxidative degradation or moisture-induced quenching.[38] The optical behaviour of ZnS QDs in thin-film form was further examined by collecting absorbance and PL spectra, as presented in Figure 12. As expected for strongly scattering nanocomposite films, the absorbance traces show no distinct excitonic features; the only resolved bands originate from the PVK matrix itself and are unrelated to the ZnS nanocrystals. The excitation maxima of the films remain essentially unchanged compared with the colloidal dispersions (≈320 nm), indicating that the band-edge absorption is largely preserved upon film formation.

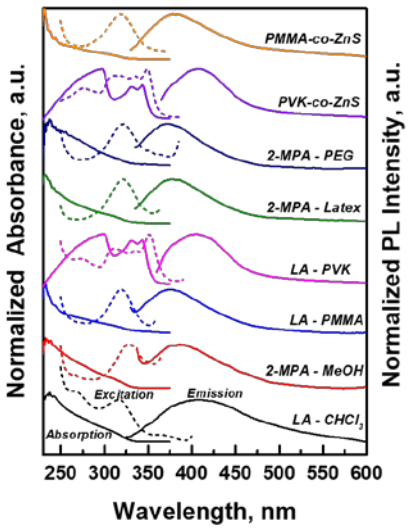

Figure 12. Normalized ABS and PL spectra of the prepared nanocomposite (ZnS QDs in polymer matrix/solvent) thin films.

In contrast, the emission spectra reveal a clear and systematic blue shift for all thin-film samples relative to their corresponding solutions. While the colloidal QDs emit around 440 nm, the photoluminescence maxima of the films fall within the 380-410 nm range. This shift reflects changes in the local dielectric environment surrounding the nanocrystals and the degree of polymer-QD interaction. More polar matrices, such as

PMMA and latex, induce a stronger blue shift, whereas less polar environments, such as PVK, lead to a more moderate shift. This behaviour is consistent with dielectric-confinement effects and partial modification of surface trap states upon embedding the QDs into different polymer hosts. Atomic force microscopy (AFM) was employed to examine the surface morphology of the prepared thin films and to evaluate how different ligand and polymer environments influence the nanoscale organization of the film. Most films display a uniform, densely packed topology with only minor nanoscale undulations (a few nanometres in height), consistent with well-dispersed QDs and efficient polymer encapsulation. In contrast, films prepared from 2-MPA-capped QDs in MeOH or PEG, as well as the PODM-PVK copolymer, exhibit markedly rougher surfaces. These samples contain micron-scale domains with height variations of 10-100 nm, indicative of partial phase separation or solvent-polymer incompatibility during drying. Despite their pronounced appearance in AFM images, these surface features do not significantly affect the optical properties of the films, as the PL spectra remain uniform, and no additional scattering-related artefacts are observed. Taken together, these results demonstrate that polymer integration is not merely a processing step but a decisive design element that defines the final optical and structural performance of the ZnS QD systems. By enabling controlled physical embedding as well as covalent incorporation through functional ligands, the polymer-QD architectures developed here provide a versatile and robust platform for fabricating flexible, large-area, and durable photonic coatings and optoelectronic components.

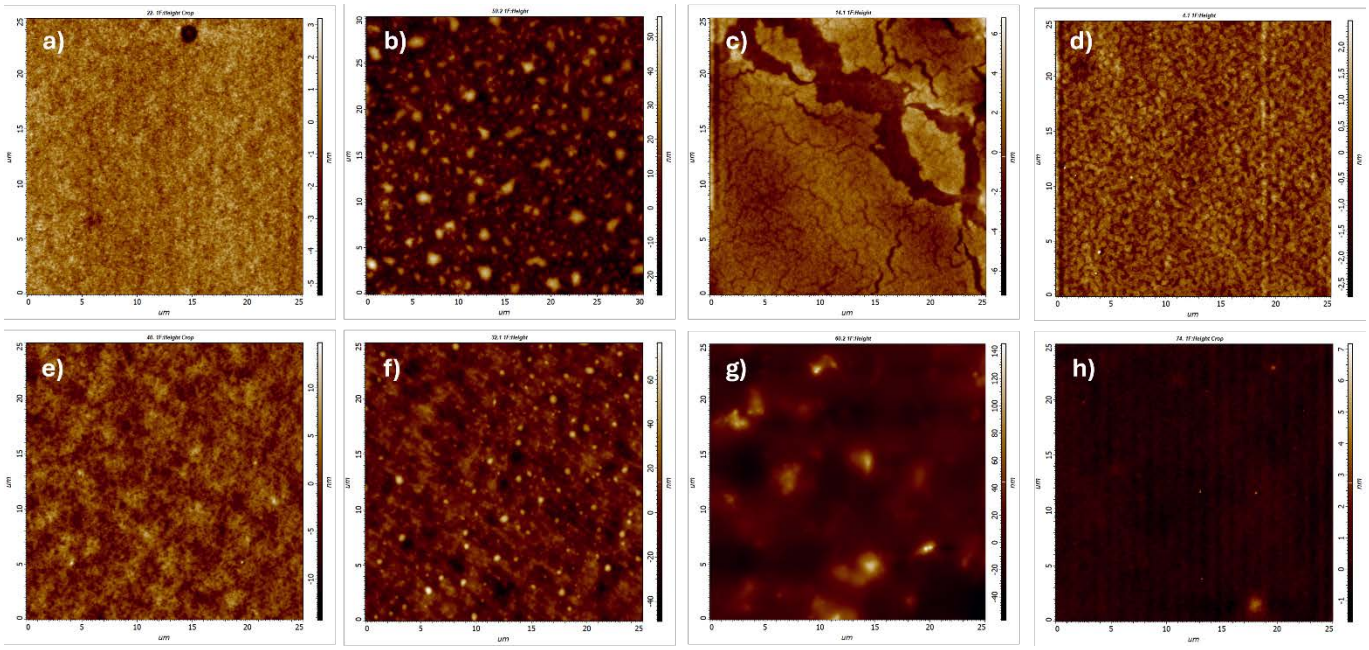

Figure 13. AFM images of the prepared ZnS QDs nanocomposites: a) ZnS/LA neat films, b) ZnS/2-MPA neat films, c) ZnS/LA dispersed in PMMA, d) ZnS/LA dispersed in PVK, e) ZnS/2-MPA dispersed in latex, f) ZnS/2-MPA dispersed in PEG, g) ZnS/PODM - PVK copolymer, and h) ZnS/BMEP - PMMA copolymer.

Conclusions

In this work, a comprehensive optical and structural investigation of ZnS quantum dots synthesized from substituted thioureas is presented, demonstrating how precursor composition, ligand architecture, and polymer environment collectively govern their photophysical behaviour. The ZnS QDs exhibit a size-dependent optical response consistent with quantum confinement, with absorption onsets in the range of 306-326 nm and optical band-gap energies of 3.55-3.77 eV.

Ligand engineering plays a decisive role in controlling exciton relaxation pathways: hydrophobic long-chain carboxylates (LA) and amphiphilic vinyl-functionalized phosphonate ligands (BMEP, PODM) effectively suppress defect-mediated non-radiative decay, whereas the compact hydrophilic ligand 2-MPA induces pronounced PL quenching due to surface trap formation.

The study further demonstrates that ligand-engineered ZnS QDs can be successfully integrated into a variety of polymer matrices, including PMMA, PVK, PEG, and methacrylate-based copolymers, either via physical dispersion or covalent grafting. This ensures good compatibility with polymer hosts, suppresses aggregation, and enables the formation of uniform emissive thin films, with dielectric confinement effects reflected in characteristic PL blue shifts and smooth film morphology confirmed by AFM.

Overall, this work establishes a versatile strategy for tuning the optical performance and processability of ZnS QDs through controlled precursor selection, ligand design, and polymer integration, providing a practical platform for photonic coatings, polymer-based nanocomposites, and optoelectronic applications based on environmentally benign ZnS nanocrystals.

Author contributions

J. J. writing - original draft, synthesis; L. L. writing - original draft, methodology, investigation, synthesis; J. J., L. L., S.S., J.R.-P., R. J., M. V., B. F., M. K., and J. H., formal analysis, data curation; M. V. and R. J., project administration. All authors edited and approved the manuscript.

Declaration of Competing Interest

The authors declare that they have no known competing financial interests or personal relationships that could have appeared to influence the work reported in this paper.

Conflicts of interest

There are no conflicts to declare.

Data availability

The datasets generated during and/or analysed during the current study are available in the Figshare repository https://doi.org/10.6084/m9.figshare.30761834.

Acknowledgements

This work has been funded by a grant from the Programme Johannes Amos Comenius under the Ministry of Education, Youth and Sports of the Czech Republic [No. CZ.02.01.01/00/23_021/0008593], and by a grant LM2023037 from the Ministry of Education, Youth and Sports of the Czech Republic.

References

1 L. Isac and A. Enesca, *Int. J. Mol. Sci*., 2022, **23**, 24, 15668; https://doi.org/10.3390/ijms232415668
2 D. Bera, L. Qian, T.-K. Tseng, and P. H. Holloway, *Materials* 2010, **3**, 4, 2260; https://doi.org/10.3390/ma3042260
3 M. A. Cotta, *ACS Appl. Nano Mater*. 2020, **3**, 6, 4920; https://doi.org/10.1021/acsanm.0c01386
4 Y. Lv, L. Zhang, R. Wu, and L. S. Li, *Nano Res*., 2024, **17**, 10309; https://doi.org/10.1007/s12274-024-6926-5
5 H. Labiadh, and S. Hidouri, *J. King Saud Univ. Sci.*, 2016, **28**, 4, 444; https://doi.org/10.1016/j.jksus.2016.12.001
6 P. P. Phadnis, H. M. Pathan, H. D. Shelke, and S. A. Kulkarni, *Proc. SPIE*, 2024, 13127; https://doi.org/10.1016/j.jksus.2016.12.001
7 S. Murugan, M. Ashokkumar, R. Kalpana Manivannan, K.J. Senthil Kumar, *Materials Today Comm*., 2025, **49**, 114032; https://doi.org/10.1016/j.mtcomm.2025.114032
8 L. Dai, R. Lesyuk, A. Karpulevich, A. Torche, G. Bester, and C. Klinke, *J. Phys. Chem. Lett*. 2019, **10**, 14, 3828; https://doi.org/10.1021/acs.jpclett.9b01466
9 Y. Wang, R. Hu, G. Lin, I. Roy, and K.-T. Yong, *ACS Appl. Mater. Interfaces*, 2013, **5**, 8, 2786; https://doi.org/10.1021/am302030a
10 X. Zhai, X. Zhang, S. Chen, W. Yang, Z. Gong, *Colloids Surf., A*, 2012, **409**, 126; https://doi.org/10.1016/j.colsurfa.2012.05.047
11 C. Cheng, B. Yu, F. Huang, L. Gao, K. Cao, P. Zang, K. Zheng, and J. Tian, Adv. Funct. Mat., 2024, **24**, 2313811; https://doi.org/10.1002/adfm.202313811
12 L. Xi, D.-Y. Cho, M. Duchamp, C. B. Boothroyd, J. Y. Lek, A. Besmehn, R. Waser, Y. M. Lam, and B. Kardynal, *ACS Appl. Mater. Interfaces*, 2014, **6**, 20, 18233; https://doi.org/10.1021/am504988j
13 G. J. J. Draaisma D. Reardon, A. P. H. J. Schenning, S. C. J. Meskers, and C. W. M. Bastiaansen, *J. Mater. Chem. C*, 2016, **4**, 5747 https://doi.org/10.1039/C6TC01261B
14 R. Shahid, M. S. Toprak, H. M. A. Soliman, and M. Muhammed, *Cent.eur.j.chem*., 2012, **10**, 54; https://doi.org/10.2478/s11532-011-0108-5;
15 A. Kaderavkova, L. Loghina, M. Chylii, S. Slang, P. Placek, B. Frumarova, and M. Vlcek, *J. Alloys Compd*., 2020, **831**, 154814; https://doi.org/10.1016/j.jallcom.2020.154814
16 L. Loghina, M. Chylii, A. Kaderavkova, S. Slang, P. Svec, J. Rodriguez-Pereira, B. Frumarova, and M. Vlcek, *Optical Materials Express*, 2021, **11**, 2, 539; https://doi.org/10.1364/OME.417371
17 L. Loghina, A. Kaderavkova, M. Chylii, B. Frumarova, P. Svec, S. Slang, and M. Vlcek, *CrystEngComm*, 2020, **22**, 4324; https://doi.org/10.1039/D0CE00597E
18 A. Iakovleva, L. Loghina, Z. Olmrova Zmrhalova, J. Mistrik, P. Svec, S. Slang, K. Palka and M. Vlcek, *J. Alloys Compd.*, 2020, **812**, 152159, https://doi.org/10.1016/j.jallcom.2019.152159
19 S. D. Pike, E. R. White, M. S. P. Shaffer, and C. K. Williams, *Nat. Comm*., 2016, **7**, 13008; https://doi.org/10.1038/ncomms13008;
20 M. Czakler, C. Artner, U. Schubert, *EurJIC*, 2013, **2013**, 5790; https://doi.org/10.1002/ejic.201300859
21 Y. Jin, D. Kishpaugh, C. Liu, T. J. Hajagos, Q. Chen, L. Li, Y. Chen, and Q. Pei, *J. Mater. Chem. C*, 2016, **4**, 3654; https://doi.org/10.1039/C6TC00447D
22 W. Ma, L. Han, Y. Xie, Q. Li, S. Xu, and C. Geng, *J. Phys. Chem. Lett*., 2025, **16**, 37, 9708; https://doi.org/10.1021/acs.jpclett.5c02363
23 G. Socrates. Infrared and Raman Characteristic Group Frequencies: Tables and Charts. *John Wiley & Sons*, 2004.
24 A. Ouasri, A. Rhandour, M. C. Dhamelincourt, P. Dhamelincourt, and A. Mazzah, *Spectrochimica Acta Part A: Molecular and Biomolecular Spectroscopy*, 2002, **58**, 12, 2779; https://doi.org/10.1016/S1386-1425(02)00019-7
25 S. Ouni, N. B. H. Mohamed, M. Bouzidi, A. Bonilla-Petriciolet, and M. Haouari, *Journal of Environmental Chemical Engineering*, 2021, **9**, 5, 105915; https://doi.org/10.1016/j.jece.2021.105915
26 N. Dengo, A. Vittadini, M. M. Natile, and S. Gross, *J. Phys. Chem. C,* 2020, **124**, 14, 7777; https://doi.org/10.1021/acs.jpcc.9b11323;
27 L. Loghina, M. Chylii, A. Kaderavkova, S. Slang, P. Svec, J. Rodriguez-Pereira, B. Frumarova, M. Cieslar and M. Vlcek, Nanomaterials, 2021, 11, 2616; https://doi.org/10.3390/nano11102616
28 M. Timpel, M. V. Nardi, S. Krause, G. Ligorio, C. Christodoulou, L. Pasquali, A. Giglia, J. Frisch, B. Wegner, P. Moras, and N. Koch, *Chem. Mater*., 2014, **26**, 17, 5042; https://doi.org/10.1021/cm502171m;
29 B. Zhang, T. Kong, W. Xu, R. Su, Y. Gao, and G. Cheng, *Langmuir*, 2010, **26**, 6, 4514; https://doi.org/10.1021/la9042827
30 A. A. Zarandi, A.A. S. Alvani, R. Salimi, H. Sameie, S. Moosakhani, M. Taherian, H.R. Hedayati, and S. Kiani, *OSA Technical Digest*, paper JW6A.33; https://doi.org/10.1364/E2.2014.JW6A.33;
31 P. Rani, R. Singh, and S. Srivastava, *Materials Today: Proceedings*, 2021, **46**, 12, 5817; https://doi.org/10.1016/j.matpr.2021.02.726

32 J. Tauc, A. Menth, *Journal of Non-Crystalline Solids*, 1972, **8**, 10, 569; https://doi.org/10.1016/0022-3093(72)90194-9

33 A. A. P. Mansur, H. S. Mansur, R. L. Mansur, F. G. de Carvalho, S. M. Carvalho, *Spectrochimica Acta Part A: Molecular and Biomolecular Spectroscopy*, 2018, **189**, 15, 393; https://doi.org/10.1016/j.saa.2017.08.049

34 J. D. Levine and P. Mark, *Phys. Rev*., 1966, **144**, 751; https://doi.org/10.1103/PhysRev.144.751

35 Y. Wang, X. Liang, X. Ma, Y. Hu, X. Hu, X. Li, and J. Fan, *Applied Surface Science*, 2014, **316**, 15, 54; https://doi.org/10.1016/j.apsusc.2014.07.135

36 S. Vempati, Y. Ertas, and T. Uyar, *J. Phys. Chem. C*, 2013, **117**, 41, 21609; https://doi.org/10.1021/jp408160h

37 J. Z. Mbese and P. A. Ajibade, *Polymers*, 2014, **6**, 9, 2332; https://doi.org/10.3390/polym6092332

38 C. Lü, Z. Cui, Y. Wang, Z. Li, C. Guan, B. Yang, and J. Shen, *J. Mater. Chem.*, 2003, **13**, 2189. https://doi.org/10.1039/B304154A